

## PERTURBATION THEORY OF THE COSMOLOGICAL LOG-DENSITY FIELD

XIN WANG<sup>1,2,3</sup>, MARK NEYRINCK<sup>2</sup>, ISTVÁN SZAPUDI<sup>4</sup>, ALEX SZALAY<sup>2</sup>, XUELEI CHEN<sup>1,5</sup>,  
JULIEN LESGOURGUES<sup>6,7</sup>, ANTONIO RIOTTO<sup>6,8</sup>, MARTIN SLOTH<sup>6</sup>

<sup>1</sup> *Key Laboratory of Optical Astronomy, National Astronomical Observatories,  
Chinese Academy of Sciences, Beijing 100012, China*

<sup>2</sup> *Department of Physics and Astronomy, Johns Hopkins University, Baltimore, MD 21218, US*

<sup>3</sup> *Graduate School of Chinese Academy of Sciences, Beijing 100049, China*

<sup>4</sup> *Institute for Astronomy, University of Hawaii, 2680 Woodlawn Dr., HI 96822, US*

<sup>5</sup> *Center of High Energy Physics, Peking University, Beijing 100871, China*

<sup>6</sup> *CERN, PH-TH Division, CH-1211, Geneva 23, Switzerland*

<sup>7</sup> *ITP, EPFL, CH-1015 Lausanne, Switzerland.*

<sup>8</sup> *INFN, Sezione di Padova, Via Marzolo 8, I-35131 Padua, Italy*

*Draft version August 21, 2021*

### ABSTRACT

The matter density field exhibits a nearly lognormal probability density distribution (PDF) after entering into the nonlinear regime. Recently, it has been shown that the shape of the power spectrum of a logarithmically transformed density field is very close to the linear density power spectrum, motivating an analytic study of it. In this paper, we develop cosmological perturbation theory for the power spectrum of this field. Our formalism is developed in the context of renormalized perturbation theory, which helps to regulate the convergence behavior of the perturbation series, and of the Taylor-series expansion we use of the logarithmic mapping. This approach allows us to handle the critical issue of density smoothing in a straightforward way. We also compare our perturbative results with simulation measurements.

*Subject headings:* cosmology: theory — large-scale structure of universe

## 1. INTRODUCTION

The large-scale structure of the Universe is typically quantified with the overdensity field. This is for good reason; the overdensity field  $\delta(\mathbf{x}) = \rho(\mathbf{x})/\bar{\rho} - 1$  (with  $\rho$  the density) seems to be essentially a Gaussian random field at early epochs, and also  $\delta$  sources the gravitational potential in the cosmological Poisson equation. However, when fluctuations are large at late times and small scales,  $\delta$  acquires some inconvenient features. It cannot go below  $-1$ , but becomes arbitrarily large in non-linear structures; this in itself forces non-Gaussianities when fluctuations become large.

On small scales and late times, the probability density distribution (PDF) of the density field has a roughly lognormal form. This was noticed regarding the galaxy density field by e.g. Hubble (1934) and Hamilton (1985). Coles & Jones (1991) explored the theoretical origins of the roughly lognormal nature of the matter density field. A lognormal model for the density field shows many features of the true nonlinear density field, such as the constraint that  $\delta$  cannot go below  $-1$ . As they showed, the continuity equation can be simplified by considering a logarithmic transformation of the density field  $A(\mathbf{x}, \tau) = \ln[1 + \delta(\mathbf{x}, \tau)]$ ,

$$\frac{dA(\mathbf{x}, \tau)}{d\tau} = \frac{d \ln[1 + \delta(\mathbf{x}, \tau)]}{d\tau} = -\nabla \cdot \mathbf{u}(\mathbf{x}, \tau) = -\theta(\mathbf{x}, \tau). \quad (1)$$

Here the Lagrangian total time derivative  $d/d\tau = \partial/\partial\tau + \mathbf{u} \cdot \nabla$ ,  $\theta = \nabla \cdot \mathbf{v}$ ,  $\tau$  is the conformal time, and  $\mathbf{u}$  is the peculiar velocity. This equation is about as simple as one could hope for, although some complexity is hidden in the mismatch between the Lagrangian time derivative and the Eulerian divergence. In the limit that  $\theta$  grows according to linear theory, given Gaussian initial conditions, this predicts an exactly lognormal PDF for particle overdensities. Indeed, the velocity field remains close to Gaussian even when the density field enters the nonlinear regime (e.g. Kofman et al. 1994), giving a nearly lognormal PDF for  $\delta$ .

$A$  is also a natural density variable in Schrödinger perturbation theory (Szapudi & Kaiser 2003), in which tree-level perturbation theory for  $A$  corresponds to partial loop summation to infinite order in  $\delta$ . This apparently captures the most important terms, explaining most of the Eulerian perturbation theory loop-level variance in  $\delta$ .

Recently, Neyrinck et al. (2009) analyzed the power spectrum of  $A$  in the high-resolution Millennium simulation (Springel et al. 2005). Neyrinck et al. (2009) found the nonlinearities in both the shape and covariance matrix of the  $A$  power spectrum to be dramatically reduced compared to the conventional  $\delta$  power spectrum. The shape of the  $A$  power spectrum seems intriguingly close to linear theory down to  $k \sim 1 h \text{ Mpc}^{-1}$ , with  $\delta$  smoothed onto a  $2-h^{-1} \text{ Mpc}$  grid. There are a few possible reasons for this near-linearity of the  $A$  power spectrum. It could be understandable with perturbation theory, a possibility which we begin to explore in this paper. It could be linked with the suppression of density peaks in regions that have undergone shell crossing. Or, it could just be a coincidence of particular aspects of a  $\Lambda\text{CDM}$ -like power spectrum, e.g. the small-scale slope.

In this paper, we make the first perturbative prediction for the  $A$  power spectrum. There are reasons to think that perturbation theory for  $A$  might work even better than for  $\delta$ . At small scales, the variance in  $A$  is much smaller than in  $\delta$  in the nonlinear regime. Also, it is tempting to try to exploit the simplicity of Eq. (1) in a Lagrangian approach.

However, working with  $A$  also presents some challenges. For the  $\delta$  field, smoothing (onto a grid, for example) has fairly trivial effects; at large scales, it leaves phases intact and dampens amplitudes negligibly. But smoothing is crucial to consider for  $A$ , giving different large-scale biases for different smoothing scales (Neyrinck et al. 2009). It is quite difficult to model final-conditions Eulerian smoothing using Lagrangian variables; this is why we use an Eulerian approach. For this, we use a Taylor series expansion of the logarithm; the slow convergence of this alternating series in itself portends low accuracy at highly nonlinear scales where  $\delta$  is large.

Despite these challenges, the perturbative calculations we present below achieve good agreement with simulation measurements. In the next section, we review the basic framework of Eulerian dynamics and discuss the logarithmic transformation. We calculate the power spectrum of the  $A$  field in standard perturbation theory in section 3, and in renormalized perturbation theory in section 4. In section 5, we present our calculation and compare it with simulation, and we conclude in section 6.

## 2. EULERIAN DYNAMICS AND THE LOGARITHMIC TRANSFORMATION

The gravitational dynamics of a pressureless fluid before shell crossing is governed by the continuity, Euler, and Poisson equations.

$$\begin{aligned} \frac{\partial \delta(\mathbf{x}, \tau)}{\partial \tau} + \nabla \cdot [ (1 + \delta(\mathbf{x}, \tau)) \mathbf{u}(\mathbf{x}, \tau) ] &= 0, \\ \frac{\partial \mathbf{u}(\mathbf{x}, \tau)}{\partial \tau} + \mathcal{H}(\tau) \mathbf{u}(\mathbf{x}, \tau) + \mathbf{u}(\mathbf{x}, \tau) \cdot \nabla \mathbf{u}(\mathbf{x}, \tau) &= -\nabla \Phi_N(\mathbf{x}, \tau) \\ \nabla^2 \Phi_N(\mathbf{x}, \tau) &= \frac{3}{2} \Omega_m(\tau) \mathcal{H}^2(\tau) \delta(\mathbf{x}, \tau). \end{aligned} \quad (2)$$

Here,  $\mathcal{H} = d \ln a(\tau)/d \ln \tau$  is the Hubble expansion rate,  $a(\tau)$  is the scale factor,  $\Omega_m(\tau)$  is the ratio of matter density to critical density, and  $\Phi_N(\mathbf{x}, \tau)$  is the Newtonian potential. In principle, perturbation theory of the log-density field is possible using the log-continuity equation, Eq. (1), together with the last two equations in Eq. (2). However, we found it more straightforward to take smoothing into account if we expand  $A$  in terms of  $\delta$ , so this is the approach that we take.

### 2.1. Equation of Motion and Perturbation Theory

First we briefly review results for the conventional overdensity field  $\delta$ . Following Crocce & Scoccimarro (2006a,b), the equation of motion in Fourier space can be written in a compact form by defining the two-component variable

$$\Psi_a(\mathbf{k}, \eta) = (\Psi_\rho(\mathbf{k}, \eta), \Psi_v(\mathbf{k}, \eta)) = (\delta(\mathbf{k}, \eta), -\theta(\mathbf{k}, \eta)/\mathcal{H}). \quad (3)$$

The index  $a \in \{\rho, v\}$  stands for density or velocity variables, respectively. Where numbered indices are more convenient, we also use  $a \in \{1, 2\}$ , i.e.  $\Psi_1 = \Psi_\rho$ , and  $\Psi_2 = \Psi_v$ .

The equation of motion then reads

$$\partial_\eta \Psi_a(\mathbf{k}, \eta) + \Omega_{ab} \Psi_b(\mathbf{k}, \eta) = \gamma_{abc}(\mathbf{k}, \mathbf{k}_1, \mathbf{k}_2) \Psi_b(\mathbf{k}_1, \eta) \Psi_c(\mathbf{k}_2, \eta), \quad (4)$$

with the convention that repeated Fourier arguments are integrated over. The time  $\eta = \ln a(\tau)$  in a Einstein-de Sitter (EdS) universe. Here the constant matrix

$$\Omega_{ab} = \begin{bmatrix} 0 & -1 \\ -3/2 & 1/2 \end{bmatrix}, \quad (5)$$

derived for an EdS universe, is still applicable in other cosmologies with negligible corrections to the coefficients, using  $\eta = \ln D(\tau)$  (with  $D$  the growth factor).

The symmetrized vertex matrix  $\gamma_{abc}$  is given by

$$\begin{aligned} \gamma_{222}(\mathbf{k}, \mathbf{k}_1, \mathbf{k}_2) &= \delta_D(\mathbf{k} - \mathbf{k}_1 - \mathbf{k}_2) \frac{|\mathbf{k}_1 + \mathbf{k}_2|^2 (\mathbf{k}_1 \cdot \mathbf{k}_2)}{2k_1^2 k_2^2} \\ \gamma_{121}(\mathbf{k}, \mathbf{k}_1, \mathbf{k}_2) &= \delta_D(\mathbf{k} - \mathbf{k}_1 - \mathbf{k}_2) \frac{(\mathbf{k}_1 + \mathbf{k}_2) \cdot \mathbf{k}_1}{2k_1^2} \end{aligned} \quad (6)$$

$\gamma_{112}(\mathbf{k}, \mathbf{k}_1, \mathbf{k}_2) = \gamma_{121}(\mathbf{k}, \mathbf{k}_2, \mathbf{k}_1)$ , and  $\gamma = 0$  otherwise.

Then the formal integral solution to Eq. (4) can be derived as

$$\Psi_a(\mathbf{k}, \eta) = g_{ab}(\eta) \phi_b(\mathbf{k}) + \int_0^\eta d\eta' g_{ab}(\eta - \eta') \gamma_{bcd}(\mathbf{k}, \mathbf{k}_1, \mathbf{k}_2) \Psi_c(\mathbf{k}_1, \eta') \Psi_d(\mathbf{k}_2, \eta') \quad (7)$$

where  $\phi_a(\mathbf{k})$  denotes the initial condition  $\phi_a(\mathbf{k}) \equiv \Psi_a(\mathbf{k}, \eta = 0)$ , and the linear propagator  $g_{ab}(\eta)$  is given by

$$g_{ab}(\eta) = \frac{e^\eta}{5} \begin{bmatrix} 32 \\ 32 \end{bmatrix} - \frac{e^{-3\eta/2}}{5} \begin{bmatrix} -2 & 2 \\ 3 & -3 \end{bmatrix}. \quad (8)$$

In the following, we adopt growing-mode initial conditions  $\phi_a(\mathbf{k}) = \delta_0(\mathbf{k}) u_a$ . Here  $u_a = (1, 1)$  is a unit vector.

A perturbative solution to Eq. (7) is then obtained by expanding in terms of initial fields

$$\begin{aligned} \Psi_a(\mathbf{k}, \eta) &= \sum_{n=1}^{\infty} \Psi_a^{(n)}(\mathbf{k}, \eta) \\ \Psi_a^{(n)}(\mathbf{k}, \eta) &= \int d^3 \mathbf{q}_{1\dots n} \delta_D(\mathbf{k} - \mathbf{q}_{1\dots n}) \mathcal{F}_{ab_1\dots b_n}^{(n)}(\mathbf{q}_1, \dots, \mathbf{q}_n; \eta) \phi_{b_1}(\mathbf{q}_1) \cdots \phi_{b_n}(\mathbf{q}_n) \end{aligned} \quad (9)$$

where  $d^3 \mathbf{q}_{1\dots n}$  is short for  $d^3 \mathbf{q}_1 \cdots d^3 \mathbf{q}_n$ , and  $\mathbf{q}_{1\dots n}$  denotes  $\mathbf{q}_1 + \cdots + \mathbf{q}_n$ . The kernels  $\mathcal{F}^{(n)}$  are fully symmetric functions of the wave vectors. As shown in Crocce & Scoccimarro (2006b), they can be obtained in terms of  $g_{ab}$  and  $\gamma_{abc}$  recursively.

$$\begin{aligned} \mathcal{F}_a^{(n)}(\mathbf{k}_1, \dots, \mathbf{k}_n; \eta) \delta_D(\mathbf{k} - \mathbf{k}_{1\dots n}) &= \left[ \sum_{m=1}^n \int_0^\eta d\eta' g_{ab}(\eta - \eta') \gamma_{bcd}(\mathbf{k}, \mathbf{k}_{1\dots m}, \mathbf{k}_{m+1\dots n}) \mathcal{F}_c^{(m)}(\mathbf{k}_{1\dots m}; \eta') \right. \\ &\quad \left. \times \mathcal{F}_c^{(n-m)}(\mathbf{k}_{m+1\dots n}; \eta') \right]_{\text{symmetrized}} \end{aligned} \quad (10)$$

For  $n = 1$ ,  $\mathcal{F}_a^{(1)}(\eta) = g_{ab}(\eta) u_b$ . It should be noted that in this formalism, the kernel depends on the time  $\eta$ , since it includes subleading terms in  $e^\eta$  (Crocce & Scoccimarro 2006a). If one only considers the fastest-growing mode,  $\mathcal{F}_a^{(n)}(\eta)$  equals the well-known PT kernel  $\exp(n\eta) \{F^{(n)}, G^{(n)}\}$ .

### 2.2. Logarithmic Transformation of the Field

In general, one can define a new vector  $\Phi_a$  as a nonlinear transformation  $\mathcal{T}$  of  $\Psi_a$ ,  $\Phi_a(\mathbf{k}, \eta) = (\Phi_\rho(\mathbf{k}, \eta), \Phi_v(\mathbf{k}, \eta)) = \mathcal{T}[\Psi_a(\mathbf{k}, \eta)]$ . In this paper, we consider a logarithmic transformation of the density field in configuration space, with  $\Phi_\rho(\mathbf{x}, \eta) = \ln[1 + \Psi_\rho(\mathbf{x}, \eta)]$ , leaving the velocity field unchanged, i.e.  $\Phi_v(\mathbf{x}, \eta) = \Psi_v(\mathbf{x}, \eta)$ .

$$\begin{aligned}\Phi_\rho(\mathbf{k}, \eta) &= A(\mathbf{k}, \eta) = \mathcal{L}[A(\mathbf{x}, \eta)] = \sum_{n=1}^{\infty} \frac{(-1)^{n+1}}{n} [\Psi_\rho * \dots * \Psi_\rho](\mathbf{k}, \eta) \\ &= \sum_{n=1}^{\infty} \frac{(-1)^{n+1}}{n} \int d^3 \mathbf{q}_{1\dots n} \delta_D(\mathbf{k} - \mathbf{q}_{1\dots n}) \Psi_\rho(\mathbf{q}_1, \eta) \dots \Psi_\rho(\mathbf{q}_n, \eta),\end{aligned}\quad (11)$$

where  $\mathcal{L}$  represents a Fourier transform, and  $*$  denotes a convolution of overdensity fields. In the following, we will interchangeably use  $\Psi_\rho$  and  $\delta$ ,  $\Phi_\rho$  and  $A$  when the meaning should be clear from context. Substituting the perturbative series expression of  $\Psi_\rho(\mathbf{q}, \eta)$  Eq. (9) into Eq. (11), we get the formal expression of  $\Phi_\rho(\mathbf{k}, \eta)$  in terms of the initial density field

$$\begin{aligned}\Phi_\rho(\mathbf{k}, \eta) &= \sum_{n=1}^{\infty} \frac{(-1)^{n+1}}{n} \int d^3 \mathbf{k}_{1\dots n} \delta_D(\mathbf{k} - \mathbf{k}_{1\dots n}) \sum_{m_1, \dots, m_n} \int d^3 \mathbf{p}_{1\dots m_1}^1 \dots d^3 \mathbf{p}_{1\dots m_n}^n \\ &\quad \delta_D(\mathbf{k}_1 - \mathbf{p}_{1\dots m_1}^1) \dots \delta_D(\mathbf{k}_n - \mathbf{p}_{1\dots m_n}^n) \mathcal{F}_{\rho b_1^1 \dots b_{m_1}^1}^{(m_1)}(\mathbf{p}_1^1, \dots, \mathbf{p}_{m_1}^1; \eta) \dots \mathcal{F}_{\rho b_1^n \dots b_{m_n}^n}^{(m_n)}(\mathbf{p}_1^n, \dots, \mathbf{p}_{m_n}^n; \eta) \\ &\quad \phi_{b_1^1}(\mathbf{p}_1^1) \dots \phi_{b_{m_1}^1}(\mathbf{p}_{m_1}^1) \times \dots \times \phi_{b_1^n}(\mathbf{p}_1^n) \dots \phi_{b_{m_n}^n}(\mathbf{p}_{m_n}^n).\end{aligned}\quad (12)$$

With this definition, it is possible to express  $\Phi_\rho(\mathbf{k})$  in a diagrammatic way. As depicted in Fig.(1), each diagram contains two levels of interactions. The thick solid  $n$ -branch tree represents the nonlinear convolution, i.e. the integration in Eq. (11), and their interaction vertex, shown as a solid square, carries a Taylor expansion coefficient  $(-1)^{n+1}/n$ , where  $n$  is the number of branches. Each branch right after the grey square represents one nonlinearly evolved density contrast  $\Psi_\rho(\mathbf{k}_n, \eta)$  at time  $\eta$ , which is followed by another  $m$  thin branches, to express its gravitational nonlinearity in terms of initial fields and perturbative kernels  $\mathcal{F}^{(m)}$ . At the end of each branch, small open circles represent the initial conditions  $\phi$ . In short, in this diagrammatic representation, we just combine  $n$  conventional diagrams representing  $\Psi_\rho$  (e.g. diagrams at the right of Fig. 2 in Bernardeau et al. (2008)) and glue them together at the solid square. When expanding  $\Phi_\rho(\mathbf{k}, \eta)$  to different orders, one should also include the information about the number of topologically equivalent diagrams, which essentially comes from the multinomial coefficient of  $(\Psi_\rho)^n$ . The final field  $\Phi_\rho(\mathbf{k}, \eta)$  is then a summation of all possible diagrams.

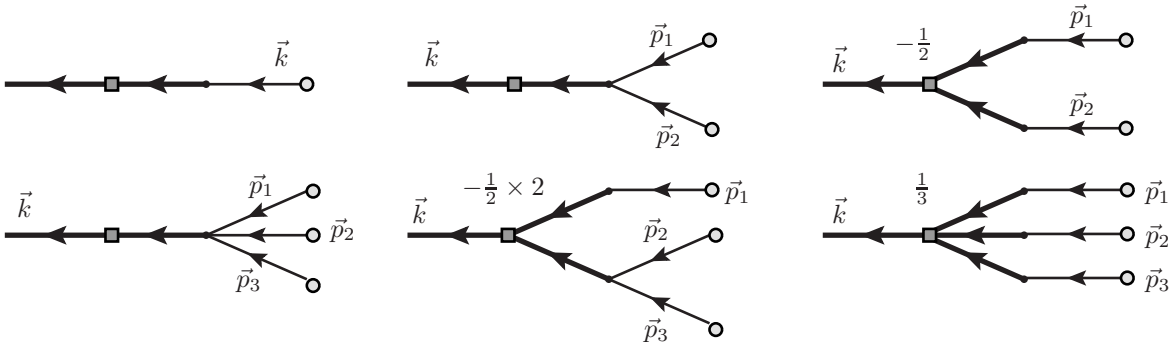


**Figure 1.** Diagrammatic representation of  $\Phi_\rho(\mathbf{k}, \eta)$  up to third order. Every single branch right after the solid square represents one nonlinearly evolved density contrast  $\Psi_\rho$  and is identical to, for example, diagrams at the right of Fig. 2 in Bernardeau et al. (2008). Explicit expressions for each diagram are shown in Eq. (15) and (16).

The power spectrum  $P_{\Phi_\rho}(k, \eta)$  is defined as

$$P_{\Phi_\rho}(k, \eta) \delta_D(\mathbf{k} + \mathbf{k}') = P_A(k, \eta) \delta_D(\mathbf{k} + \mathbf{k}') = \langle \Phi_\rho(\mathbf{k}, \eta) \Phi_\rho(\mathbf{k}', \eta) \rangle \quad (13)$$

In this paper, we assume Gaussian initial conditions, with all the statistical information encoded in the initial power spectrum

$$\langle \phi_a(\mathbf{k}) \phi_b(\mathbf{k}') \rangle = \delta_D(\mathbf{k} + \mathbf{k}') P_{ab}(k), \quad (14)$$

where  $P_{ab}(k) = u_a u_b P_0(k)$  for growing-mode initial conditions. Diagrammatically, the ensemble average is obtained by gluing two open circles together to form the symbol  $\otimes$ , which represents the initial power spectrum  $P_{ab}(k)$ .

Before proceeding, let's examine the definition of  $\Phi_\rho$  carefully. The overdensity can be idealized as a continuous field. In practice, however, estimating a density field from points (galaxies or simulation particles) requires a choice of a finite resolution, effectively a smoothing length. Furthermore, since the value of density field  $\Psi_\rho(\mathbf{x})$  strongly depends on the scale of the smoothing, as we will see, the resultant field as well as its statistical properties also vary according to the smoothing procedure adopted. In the following, we will consider the density field  $\Psi_\rho$  smoothed by a spherical top-hat window function with radius  $R$ .

### 3. STANDARD PERTURBATION THEORY

Given the perturbation expansion of  $\Phi_\rho(\mathbf{k}, \eta)$  as well as the dynamics of the density field, it is straightforward to calculate the power spectrum of a logarithmically transformed field within the standard Eulerian perturbation theory (SPT). Up to third order, it follows from Eq. (11) and Eq. (12) that

$$\begin{aligned}\Phi_\rho(k) &= \Phi_\rho^{(1)}(k) + \Phi_\rho^{(2)}(k) + \Phi_\rho^{(3)}(k) + \dots \\ &= \Psi_\rho^{(1)}(k) + \left( \Psi_\rho^{(2)}(k) - \frac{1}{2} [\Psi_\rho^{(1)} * \Psi_\rho^{(1)}](k) \right) + \left( \Psi_\rho^{(3)}(k) - [\Psi_\rho^{(1)} * \Psi_\rho^{(2)}](k) \right. \\ &\quad \left. + \frac{1}{3} [\Psi_\rho^{(1)} * \Psi_\rho^{(1)} * \Psi_\rho^{(1)}](k) \right) + \dots\end{aligned}\quad (15)$$

As discussed previously, a smoothing procedure is usually involved in practice. Applying a spherically symmetric kernel  $W(kR)$  of characteristic scale  $R$ , we get

$$\begin{aligned}\Phi_\rho^{(1)}(k) &= \Psi_\rho^{(1)}(k)W(kR) \\ \Phi_\rho^{(2)}(k) &= \Psi_\rho^{(2)}(k)W(kR) - \frac{1}{2} \int d^3\mathbf{p} \Psi_\rho^{(1)}(p)\Psi_\rho^{(1)}(|\mathbf{k}-\mathbf{p}|) W(pR)W(|\mathbf{k}-\mathbf{p}|R) \\ \Phi_\rho^{(3)}(k) &= \Psi_\rho^{(3)}(k)W(kR) - \int d^3\mathbf{p} \Psi_\rho^{(2)}(p)\Psi_\rho^{(1)}(|\mathbf{k}-\mathbf{p}|) W(pR)W(|\mathbf{k}-\mathbf{p}|R) \\ &\quad + \frac{1}{3} \int d^3\mathbf{p}_{12} \Psi_\rho^{(1)}(p_1)\Psi_\rho^{(1)}(p_2)\Psi_\rho^{(1)}(|\mathbf{k}-\mathbf{p}_{12}|) W(p_1R)W(p_2R)W(|\mathbf{k}-\mathbf{p}_{12}|R)\end{aligned}\quad (16)$$

These expressions are shown diagrammatically in Fig. 1 ( $\Phi_\rho^{(1)}$  and  $\Phi_\rho^{(2)}$  in the top row, and  $\Phi_\rho^{(3)}$  in the bottom). Note that the smoothing is taken over the evolved nonlinear density field  $\Psi_\rho$ . The power spectrum  $P_A(k)$  is then obtained by calculating the series

$$P_A(k) = P_A^{(11)}(k) + 2 P_A^{(13)}(k) + P_A^{(22)}(k) + \dots\quad (17)$$

where  $P_A^{(ij)}(k) = \langle \Phi_\rho^{(i)}(\mathbf{k})\Phi_\rho^{(j)}(\mathbf{k}) \rangle$ . It is clear that the tree-level power spectrum  $P_A(k, \eta)$  equals exactly the one of the standard overdensity field

$$P_A^{(11)}(k, \eta) = P_\delta^{(11)}(k, \eta)W^2(kR) = D^2(\eta)W^2(kR)P_0(k),\quad (18)$$

where  $D(\eta)$  is the linear growth function, and  $P_0(k)$  is the initial power spectrum. In the following, we will also denote the linear overdensity power spectrum  $P_\delta^{(11)}(k, \eta)$  as  $P_L(k, \eta)$ . To see the crucial role played by the smoothing window function, let us calculate  $2P_A^{(13)}(k, \eta)$ .

$$\begin{aligned}2P_A^{(13)}(k, \eta) &= 2P_\delta^{(13)}(k, \eta)W^2(kR) + \int d^3\mathbf{p}_{12} \langle \delta_0(\mathbf{k})\delta_0(\mathbf{p}_1)\delta_0(\mathbf{p}_2)\delta_0(-\mathbf{k}-\mathbf{p}_{12}) \rangle \\ &\quad \times \left[ \frac{2}{3} D^4(\eta) W(kR)W(p_1R)W(p_2R)W(|\mathbf{k}+\mathbf{p}_{12}|R) - 2\mathcal{F}^{(2)}(\mathbf{p}_2, -\mathbf{k}-\mathbf{p}_{12}; \eta) \right. \\ &\quad \left. \times W(kR)W(p_1R)W(|\mathbf{k}+\mathbf{p}_1|R) \right],\end{aligned}\quad (19)$$

where  $\delta_0$  is the initial fluctuation. This can be further simplified by performing the angular part of the integration. Considering only the fastest-growing mode and assuming spherical top-hat smoothing (see Appendix A and Appendix B for more details), Eq. (19) becomes

$$\begin{aligned}2P_A^{(13)}(k, \eta) &= \left[ 2P_\delta^{(13)}(k, \eta) - \left( \frac{26}{21} + \frac{1}{3} \frac{d \ln \sigma_R^2}{d \ln R} \right) \sigma_R^2 P_L(k, \eta) \right] W_{\text{th}}^2(kR) \\ &\quad - \frac{2}{3} \sigma_R^2 P_L(k, \eta) kR W'_{\text{th}}(kR)W_{\text{th}}(kR).\end{aligned}\quad (20)$$

where the variance of the smoothed density fluctuation  $\sigma_R^2 = \int d^3\mathbf{q} P_L(q, \eta) W_{\text{th}}^2(qR)$ , and the derivative

$$\sigma_R^2 \frac{d \ln \sigma_R^2}{d \ln R} = \frac{1}{2} \int d^3\mathbf{q} P_L(q, \eta) qR W'_{\text{th}}(qR)W_{\text{th}}(qR).\quad (21)$$

Here we have used the geometric properties of the spherical top-hat window function derived by Bernardeau (1994a,b, 1996).

Since  $P_A^{(13)}$  is proportional to the linear power spectrum  $P_L$ , and it is well-known that  $(P_\delta^{(13)}/P_L)(k \rightarrow 0) \rightarrow 0$ , the power spectrum at large scales is biased with respect to the density power spectrum

$$\frac{P_L + 2P_A^{(13)}}{P_L}(k \rightarrow 0) = 1 - \left( \frac{26}{21} + \frac{1}{3} \frac{d \ln \sigma_R^2}{d \ln R} \right) \sigma_R^2. \quad (22)$$

Without the smoothing term, the bias in Eq. (22) would equal  $1 - 26/21 \sigma_R^2$ . This expression accords with the first-order perturbative bias in Eq. (A2) (after expanding the cumulants) of Neyrinck et al. (2009); it is also plotted as a function of redshift in Fig. 4 of that paper. The bias becomes unphysically negative at  $z \lesssim 4$  for  $2\text{-}h^{-1}$  Mpc cells. This smoothing term increases the predicted bias, extending its range of validity to significantly smaller smoothing scales. However, we found that it still goes pathologically negative at small smoothing scales. This issue is resolved in a renormalized approach, which we describe in the next section.

#### 4. RENORMALIZED PERTURBATION THEORY

As the density fluctuations evolve into the non-linear regime at late times, the validity of standard perturbation theory breaks down. Loop contributions become ill-behaved and the convergence of perturbation series gets out of control. Several different approaches beyond SPT have been proposed recently, e.g. the renormalized perturbation theory (RPT) (Crocce & Scoccimarro 2006a,b; Bernardeau et al. 2008), the Lagrangian resummation theory (Matsubara 2008), the closure theory (Taruya & Hiramatsu 2008), and the time renormalization group theory (TRG) (Pietroni 2008). In this section, after a brief review of the RPT introduced by Crocce & Scoccimarro (2006a,b), we will show that it is possible to construct the perturbation series for the transformed density field based on the non-linear propagator of the density.

##### 4.1. Renormalized Perturbation Theory of the Overdensity Field

The crucial step of renormalized perturbation theory is to define the generalized growth factor, known as the propagator  $G_{ab}(k)$

$$G_{ab}(k, \eta) \delta_D(\mathbf{k} - \mathbf{k}') = \Gamma_{\Psi_{ab}}^{(1)}(k, \eta) \delta_D(\mathbf{k} - \mathbf{k}') \equiv \left\langle \frac{\delta \Psi_a(\mathbf{k}, \eta)}{\delta \phi_b(\mathbf{k}')} \right\rangle, \quad (23)$$

which effectively describes the time evolution of individual Fourier modes when non-linear mode-coupling is included. The propagator measures the dependence of a non-linearly evolved Fourier mode  $\Psi_a(\mathbf{k}, \eta)$  on its initial state  $\phi_b(\mathbf{k})$  on average. Intuitively, one should expect  $G_{ab}$  to decay to zero at small scales since non-linear mode-coupling has erased all the information from the initial state at that  $\mathbf{k}$ . Indeed, with the help of the Feynman diagrams introduced in Crocce & Scoccimarro (2006a), the dominant contribution can be summed up explicitly in the large- $k$  limit, and giving the Gaussian decay  $G_{ab}(k) = \exp(-k^2 \sigma_v^2 (a-1)^2/2)$ . In this paper, the non-linear propagator is diagrammatically presented as a grey circle with an incoming branch. It is a summation of infinite number of loop contributions, as illustrated in Fig. 2.

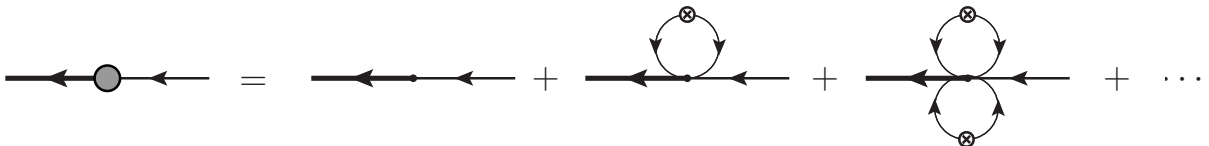


**Figure 2.** The nonlinear propagator  $\Gamma_{\Psi}^{(1)}(k, \eta)$  has an infinite number of loop contributions.

Given above, Crocce & Scoccimarro (2006a) was able to rewrite the nonlinear power spectrum as a summation of two contributions

$$P_\delta(k, \eta) = G^2(k, \eta) P_0(k) + P_{MC}(k, \eta), \quad (24)$$

where  $G$  is the density propagator  $G(k, \eta) = G_{1b} u_b$ , and  $P_{MC}(k, \eta)$  is the mode-coupling term. Therefore, the non-linear power spectrum at any  $\mathbf{k}$  is composed of two parts. One is proportional to the initial power spectrum at the same  $\mathbf{k}$ ; the other comes from mode-coupling of other  $\mathbf{k}'$ . As  $G(k)$  decays at small scales, more and more power comes from the mode-coupling contribution. Bernardeau et al. (2008) showed that these complicated mode-coupling contributions can be expressed as a summation of multi-point propagators, defined as

$$\Gamma_{\Psi_{a b_1 \dots b_n}}^{(n)}(\mathbf{k}_1, \dots, \mathbf{k}_n; \eta) \delta_D(\mathbf{k} - \mathbf{k}_{1 \dots n}) = \frac{1}{n!} \left\langle \frac{\delta^n \Psi_a(\mathbf{k}, \eta)}{\delta \phi_{b_1}(\mathbf{k}_1) \dots \delta \phi_{b_n}(\mathbf{k}_n)} \right\rangle, \quad (25)$$

which is nothing but a generalization of two-point propagator  $G_{ab}$ . When concentrating on the density contrast ( $a = \rho$ ), we will denote Eq. (25) as  $\Gamma_{\delta_{b_1 \dots b_n}}^{(n)}$  (or  $\Gamma_{\Psi_\rho_{b_1 \dots b_n}}^{(n)}$ ) for simplicity. Similarly, the dominant part of multi-point propagators can also be summed and decay into the nonlinear regime at the same rate as two-point propagator.

Bernardeau et al. (2008) showed that a simple approximation which generalizes the  $k$ -dependence of two-point propagators agrees with the data with acceptable accuracy,

$$\Gamma_{\Psi}^{(n)}(\mathbf{k}_1, \dots, \mathbf{k}_n; \eta) = \frac{\Gamma_{\Psi}^{(1)}(|\mathbf{k}_{1\dots n}|)}{\Gamma_{\Psi}^{(1, \text{tree})}(|\mathbf{k}_{1\dots n}|)} \Gamma_{\Psi}^{(n, \text{tree})}(\mathbf{k}_1, \dots, \mathbf{k}_n; \eta), \quad (n \geq 2). \quad (26)$$

With Eq. (25), the nonlinear power spectrum can then be expressed as

$$P_{\Psi ab}(k, \eta) = \sum_{r \geq 1} r! \int d^3 \mathbf{q}_{1\dots r} \delta_D(\mathbf{k} - \mathbf{q}_{1\dots r}) \Gamma_{\Psi a}^{(r)}(\mathbf{q}_1, \dots, \mathbf{q}_r; \eta) \Gamma_{\Psi b}^{(r)}(\mathbf{q}_1, \dots, \mathbf{q}_r; \eta) P_0(q_1) \cdots P_0(q_r). \quad (27)$$

$P_{MC}$  is the summation of all terms  $r \geq 2$ . For density fluctuations, it reads up to one-loop order

$$P_{\delta}(k, \eta) = \left[ \Gamma_{\delta}^{(1)}(k; \eta) \right]^2 P_0(k) + 2 \int d^3 \mathbf{q} \left[ \Gamma_{\delta}^{(2)}(\mathbf{k} - \mathbf{q}, \mathbf{q}; \eta) \right]^2 P_0(|\mathbf{k} - \mathbf{q}|) P_0(q) \quad (28)$$

Note that Eq. (27) describes nothing but an alternative way of taking ensemble averages, or diagrammatic speaking, gluing initial states. Instead of gluing two density fields order by order, one can first construct the objects by gluing initial states of individual density fields with  $n$  incoming branches, known as an  $(n+1)$ -point propagator, and the final non-linear power spectrum is then obtained by gluing two propagators together. With this observation, we can generalize this renormalization method to the perturbation theory of log-transformed fields.

#### 4.2. Renormalized Perturbation Theory of the Log-Density Field

In this section, we apply the renormalized perturbation theory Eq. (25, 27) to the log-transformed field  $\Phi_{\rho}$ . One can define the  $(n+1)$ -point nonlinear propagator  $\Gamma_{\Phi}^{(n)}$  of  $\Phi_a$ ,

$$\Gamma_{\Phi ab_1\dots b_n}^{(n)}(\mathbf{k}_1, \dots, \mathbf{k}_n; \eta) \delta_D(\mathbf{k} - \mathbf{k}_{1\dots n}) = \frac{1}{n!} \left\langle \frac{\delta^n \Phi_a(\mathbf{k})}{\delta \phi_{b_1}(\mathbf{k}_1) \cdots \delta \phi_{b_n}(\mathbf{k}_n)} \right\rangle. \quad (29)$$

For  $\Phi_{\rho}$ , we will denote  $\Gamma_{A b_1\dots b_n}^{(n)}$  or  $\Gamma_{\Phi_{\rho} b_1\dots b_n}^{(n)}$ . Unlike its counterpart  $\Gamma_{\Psi}^{(n)}$ ,  $\Gamma_{\Phi}^{(n)}$  encodes not only the nonlinear information of gravitational evolution, but also of the transformation. Substituting the perturbation series of  $\Phi_{\rho}$  Eq. (11) into Eq. (29), one notices that  $\Gamma_{\Phi}^{(n)}$  can be expanded in terms of the number of  $\Psi_{\rho}$  involved. That is,  $\Gamma_{\Phi ab_1\dots b_n}^{(n, p)} = \sum_p \Gamma_{\Phi ab_1\dots b_n}^{(n, p)}$ , where

$$\Gamma_{\Phi ab_1\dots b_n}^{(n, p)}(\mathbf{k}_1, \dots, \mathbf{k}_n; \eta) \delta_D(\mathbf{k} - \mathbf{k}_{1\dots n}) = \frac{(-1)^{p+1}}{n! p} \int d^3 \mathbf{q}_{1\dots p} \delta_D(\mathbf{k} - \mathbf{q}_{1\dots p}) \left\langle \frac{\delta^n}{\delta \phi_{b_1}(\mathbf{k}_1) \cdots \delta \phi_{b_n}(\mathbf{k}_n)} \right. \\ \left. [\Psi_{\rho}(\mathbf{q}_1, \eta) \cdots \Psi_{\rho}(\mathbf{q}_p, \eta)] \right\rangle. \quad (30)$$

In Fig.(3), we depict the expansion for the two-point propagator. The dark ellipse here represents the complicated ensemble average in Eq. (30). Note the Taylor coefficient of the logarithmic transformation carried by each diagram.

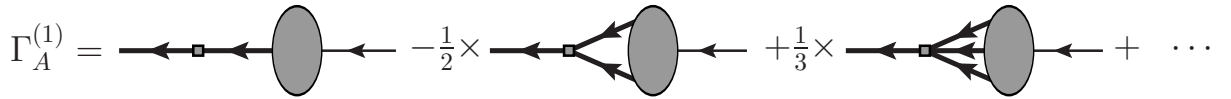


**Figure 3.** Diagrammatic demonstration of the expansion of the two-point nonlinear propagator  $\Gamma_A^{(1)}$  (Eq. 30). The terms on the RHS correspond to contributions from  $n = 1$  and  $p = 1, 2$  and 3.

Taking the two-point propagator as an example, now let's write down all contributions formally. First of all, it is clear that the one- $\Psi_{\rho}$  term, i.e. the first diagram in Fig.(3), equals  $G(k, \eta)$ . For the two- $\Psi_{\rho}$  term, i.e.  $n = 1, p = 2$  in Eq. (30), we can use Eq. (9) to further expand  $\Psi_{\rho}$  perturbatively

$$\Gamma_{A a}^{(1, 2)}(\mathbf{k}; \eta) = -\frac{1}{2} \times 2 \int d^3 \mathbf{q}_{12} \delta_D(\mathbf{k} - \mathbf{q}_{12}) \left\langle \frac{\delta \Psi_{\rho}(\mathbf{q}_1, \eta)}{\delta \phi_a(\mathbf{k})} \Psi_{\rho}(\mathbf{q}_2, \eta) \right\rangle \\ = -\frac{1}{2} \times 2 \int d^3 \mathbf{q}_{12} \delta_D(\mathbf{k} - \mathbf{q}_{12}) \sum_{n_1, n_2} (n_1 + 1) \int d^3 \mathbf{p}_{1\dots n_1} d^3 \mathbf{p}'_{1\dots n_2} \delta_D(\mathbf{q}_1 - \mathbf{k} - \mathbf{p}_{1\dots n_1}) \\ \times \delta_D(\mathbf{q}_2 - \mathbf{p}'_{1\dots n_2}) \mathcal{F}_{\rho ac_1\dots c_{n_1}}^{(n_1+1)}(\mathbf{k}, \mathbf{p}_1, \dots, \mathbf{p}_{n_1}; \eta) \mathcal{F}_{\rho d_1\dots d_{n_2}}^{(n_2)}(\mathbf{p}'_1, \dots, \mathbf{p}'_{n_2}; \eta) \\ \times \langle \phi_{c_1}(\mathbf{p}_1) \cdots \phi_{c_{n_1}}(\mathbf{p}_{n_1}) \phi_{d_1}(\mathbf{p}'_1) \cdots \phi_{d_{n_2}}(\mathbf{p}'_{n_2}) \rangle, \quad (31)$$

where  $n_1, n_2$  are expansion indices of two density fluctuations  $\Psi_\rho$ . The coefficient  $(n_1 + 1)$  comes from the functional derivative  $\delta\Psi_\rho/\delta\phi_a$ . Note that we have integrated out the variable  $\mathbf{p}_{n_1+1}$  in the last equality together with the Dirac delta function  $\delta_D(\mathbf{p}_{n_1+1} - \mathbf{k})$ , which resulted from the functional derivative.

By Wick's theorem, the joint ensemble average in the second equality can be written in terms of combinations of two-point correlations. Each of these terms can be labeled by three indices  $r_1, r_2, t$ , where  $n_1 = 2r_1 + t$ ,  $n_2 = 2r_2 + t$ , i.e. we classify all pairs into three categories:  $r_1$  pairs within the first field  $\phi_{c_i}(\mathbf{p}_i)$ , ( $1 < i < n_1$ );  $r_2$  pairs within the second field  $\phi_{d_j}(\mathbf{p}'_j)$ , ( $1 < j < n_2$ ); and  $t$  pairs in between. The renormalization is then achieved by realizing that a pre-summation of  $r_1$  and  $r_2$  gives rise to one  $(t + 2)$ -point and another  $(t + 1)$ -point propagator. Therefore,

$$\Gamma_{A a}^{(1, 2)}(\mathbf{k}; \eta) = - \sum_n (n + 1)! \int d^3 \mathbf{p}_{1 \dots n} \Gamma_{\delta a}^{(n+1)}(\mathbf{k}, \mathbf{p}_1, \dots, \mathbf{p}_n; \eta) \Gamma_{\delta}^{(n)}(-\mathbf{p}_1, \dots, -\mathbf{p}_n; \eta) P_0(p_1) \dots P_0(p_n), \quad (32)$$

where we have introduced the notation

$$\Gamma_{\delta}^{(n)}(\mathbf{p}_1, \dots, \mathbf{p}_n; \eta) \equiv \Gamma_{\Psi_\rho}^{(n)}(\mathbf{p}_1, \dots, \mathbf{p}_n; \eta) = \Gamma_{\Psi_{\rho c_1 \dots c_n}}^{(n)}(\mathbf{p}_1, \dots, \mathbf{p}_n; \eta) u_{c_1} \dots u_{c_n}. \quad (33)$$

and used the definition of  $\Gamma_{\Psi}^{(n)}$  in terms of the perturbation kernel. The coefficient  $n!$  then comes from all possible ways of matching  $n$  initial states with another group of  $n$  initial states. It is not hard to notice the similarity between Eq. (32) and Eq. (27), since the derivations are nearly identical. Yet, there are also several differences. For the RPT description of the matter power spectrum, both propagators share the same order; otherwise, it would be impossible to match the pair. For the same reason, the order of one propagator in Eq. (32) is always greater than the other by one, since we have to select one branch out before taking the average. To conclude, we are able to construct  $\Gamma_A$  from terms involving  $\Gamma_\delta$ .

Similarly, for the three- $\Psi_\rho$  term, we have

$$\begin{aligned} \Gamma_{A a}^{(1, 3)}(\mathbf{k}; \eta) &= \sum_{n_1, n_2, n_3} g_{n_1, n_2, n_3} \int d^3 \mathbf{p}_{1 \dots n_1} d^3 \mathbf{p}'_{1 \dots n_2} d^3 \mathbf{p}''_{1 \dots n_3} \Gamma_{\delta a}^{(n_1 + n_2 + 1)}(\mathbf{k}; \mathbf{p}_1, \dots, \mathbf{p}_{n_1}; \mathbf{p}'_1, \dots, \mathbf{p}'_{n_2}; \eta) \\ &\times \Gamma_{\delta}^{(n_2 + n_3)}(-\mathbf{p}'_1, \dots, -\mathbf{p}'_{n_2}; \mathbf{p}''_1, \dots, \mathbf{p}''_{n_3}; \eta) \Gamma_{\delta}^{(n_3 + n_1)}(-\mathbf{p}''_1, \dots, -\mathbf{p}''_{n_3} - \mathbf{p}_1, \dots, -\mathbf{p}_{n_1}; \eta) \\ &\times P_0(p_1) \dots P_0(p_{n_1}) P_0(p'_1) \dots P_0(p'_{n_2}) P_0(p''_1) \dots P_0(p''_{n_3}). \end{aligned} \quad (34)$$

where, for each contribution

$$g_{n_1, n_2, n_3} = (n_1 + n_2 + 1) \binom{n_1 + n_2}{n_1} \binom{n_2 + n_3}{n_2} \binom{n_3 + n_1}{n_3} n_1! n_2! n_3! \quad (35)$$

In this case, in order to describe all configurations, we need 3 indices to label the internal pairing and another 3 indices  $(n_1, n_2, n_3)$  for pairing in between. The coefficient of each contribution  $g_{n_1, n_2, n_3}$  can be understood as the number of equivalent ways of gluing pairs given the triplet  $\mathbf{n}_c = (n_1, n_2, n_3)$ . The number of initial states for each  $\Psi_\rho$  is  $\mathbf{n}_v = (n_1 + n_2 + 1, n_2 + n_3, n_3 + n_1)$ . After selecting one initial state from the first  $\Psi_\rho$  (with  $n_1 + n_2 + 1$  possibilities), one has to count the number of choosing  $\mathbf{n}_c$  out of  $\mathbf{n}_v$ , which equals  $\binom{n_1 + n_2}{n_1} \binom{n_2 + n_3}{n_2} \binom{n_3 + n_1}{n_3}$ . The formula can be further generalized to arbitrary order  $n$ ,

$$\begin{aligned} \Gamma_{A a}^{(1, n)}(\mathbf{k}; \eta) &= \sum_{\{t_{ij}\}} g_{\{t_{ij}\}}^{(1, n)} \left\{ \int \left[ \prod_{1 \leq i < j \leq n} d^3 \mathbf{p}_{1 \dots t_{ij}}^{ij} \right] \prod_{1 \leq i < j \leq n} [P_0(p^{ij})]^{t_{ij}} \right. \\ &\times \left. \Gamma_{\delta a}^{(t_1 + 1)}(\mathbf{k}; \mathbf{p}_{1 \dots t_{11}}^{11}, \dots, \mathbf{p}_{1 \dots t_{1n}}^{1n}; \eta) \dots \Gamma_{\delta}^{(t_n)}(\mathbf{p}_{1 \dots t_{n1}}^{n1}, \dots, \mathbf{p}_{1 \dots t_{nn}}^{nn}; \eta) \right\}, \end{aligned} \quad (36)$$

where the index  $t_{ij}$  denotes the number of connections between the  $i$ -th and the  $j$ -th density field  $\Psi_\rho$  (e.g.  $\{t_{ij}\} = \{t_{12}, t_{13}, t_{14}, t_{23}, t_{24}, t_{34}\}$  for  $n = 4$ ), so the total number of the indices is then  $n(n - 1)/2$ . The coefficient  $g_{\{t_{ij}\}}^{(1, n)}$  is then

$$g_{\{t_{ij}\}}^{(1, n)} = (-1)^{n+1} \times (t_1 + 1) \left[ \prod_{1 \leq i \leq n} \binom{t_i}{t_{i1} \dots t_{in}} \right] \left[ \prod_{1 \leq i < j \leq n} (t_{ij})! \right]. \quad (37)$$

Here,  $t_i = \sum_m t_{im}$  is the total number of connections linked between the  $i$ -th density field  $\Psi_\rho$  and others, with  $t_{ij} = t_{ji}$ . Eq. (37) expresses the products of multinomial coefficients of choosing  $\{t_{i1}, \dots, t_{in}\}$  from  $t_i$  for each density field times, all possible permutations within  $t_{ij}$  for pair matching. Each connection carries a momentum  $\mathbf{p}_l^{ij}$ , ( $1 < l < t_{ij}$ ), which characterize the  $l$ -th connection between  $i$ -th  $\Psi_\rho$  and  $j$ -th  $\Psi_\rho$ . The integration is taken over momenta of all possible connections among  $n$  different density fields. Because of the ensemble average Eq. (14), we have  $\mathbf{p}_{t_{ij}}^{ij} = -\mathbf{p}_{t_{ij}}^{ji}$ . And we also used the shorthand notation  $[P_0(p^{ij})]^{t_{ij}}$  for  $P_0(p_1^{ij}) \dots P_0(p_{t_{ij}}^{ij})$ .



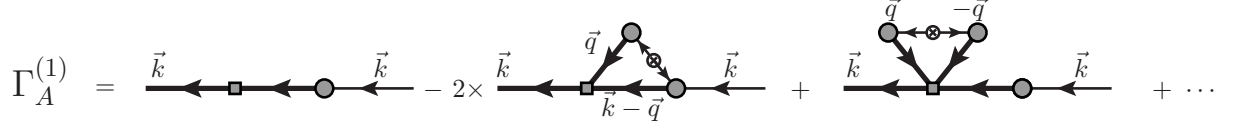


**Figure 4.** Nonlinear propagator  $\Gamma_A^{(1)}(k)$  of  $\ln(1 + \delta)$  up to one-loop order, corresponding to contributions in Eq. (38) and (39).

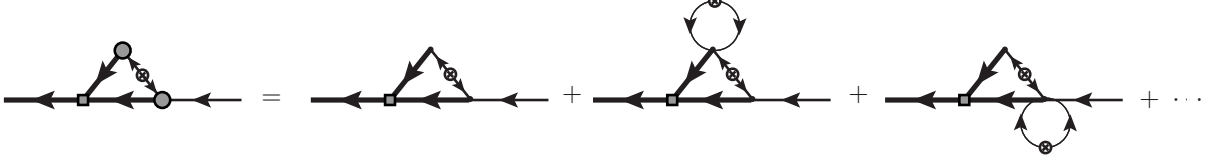


**Figure 5.** Each diagram contains an infinite number of loop contributions.

Now we can expand  $\Gamma_A^{(1)}$  in terms of the number of initial power spectra entering the calculation. For the tree level, it simply reads as

$$\Gamma_{A a}^{(1, \text{tree})}(\mathbf{k}; \eta) = \Gamma_{\delta a}^{(1)}(\mathbf{k}; \eta) W(kR) \quad (38)$$

At one-loop, from Eq. (36), the contribution would be nonzero only when  $n \leq 3$ , since otherwise there would exist at least one  $\Gamma_{\delta}$  with zeroth order, which would vanish because  $\Gamma_{\delta}^{(0)} = \langle \Psi_{\rho} \rangle = 0$ . For  $n = 2$ ,  $t_{12} = 1$ , the coefficient equals  $-2$ . For  $n = 3$ ,  $t_{23} = 1, t_{12} = t_{13} = 0$ , the coefficient equals 1. So we have

$$\begin{aligned} \Gamma_{A a}^{(1, 1\text{-loop})}(\mathbf{k}; \eta) = & \int d^3 \mathbf{q} P_0(q) \left[ \left[ W(qR) \Gamma_{\delta}^{(1)}(\mathbf{q}; \eta) \right]^2 \Gamma_{\delta a}^{(1)}(\mathbf{k}; \eta) W(kR) - 2 W(qR) W(|\mathbf{k} - \mathbf{q}|R) \right. \\ & \left. \times \Gamma_{\delta a}^{(2)}(\mathbf{k}, -\mathbf{q}; \eta) \Gamma_{\delta}^{(1)}(\mathbf{q}; \eta) \right]. \end{aligned} \quad (39)$$

Given Eq. (36), we can draw every contribution diagrammatically. Starting from the diagram representing  $\Phi_{\rho}^{(n)}$  in Fig.(1), we change all kernels into  $n$ -point propagators. After selecting one particular branch out, we glue the rest of the initial states (open circles) together. Every resultant topologically inequivalent diagram represents one or several terms in Eq. (36). Since all ordinary kernels have already been substituted by propagators, the ensemble average (gluing) is only performed among different density fields  $\Psi_{\rho}$ . In Fig.(4), we show all diagrams of  $\Gamma_A^{(1)}$  up to one-loop order. They correspond one-to-one to Eq. (38) and Eq. (39). We also present all two-loop diagrams of  $\Gamma_A^{(1)}$  in Fig.(10). It should be emphasized that, by substituting ordinary kernels into propagators, each diagram in fact contains an infinite number of loop contributions at every substituting position, as shown in Fig.(5).

For each diagram, there exists a straight path through the diagram carrying the same momentum  $\mathbf{k}$  at both the start and end. Along this path, there is one convolution vertex, as well as one  $(n + 1)$ -point propagator  $\Gamma_{\delta}^{(n)}$ . For  $n = 1$  (e.g. the third diagram in Fig.(4)), this contribution recovers the same  $k$ -dependence as  $\Gamma_{\delta}^{(1)}(k)$ , rescaled by a constant from loop integration. When  $n > 1$ , Eq. (26) suggests a similar damping of  $\mathbf{k}$  given  $\mathbf{p}_1 \cdots \mathbf{p}_{n-1}$ . Meanwhile every propagator associates with a smoothing window function  $W(kR)$ . Therefore one should expect that, in the large- $k$  limit,  $\Gamma_A^{(1)}$  will decay as a combined effect of a Gaussian damping of  $\Gamma_{\delta}^{(1)}$  and the smoothing window function. Furthermore, as we will see in the next section, the presence of the propagator within the loop helps to regulate the convergence of the numerical calculation.

One can also derive the three-point propagator similarly, except that two distinct contributions have to be taken into account because of the second derivative in the definition of  $\Gamma_A^{(2)}$ .

$$\begin{aligned} \Gamma_{A ab}^{(2, n)}(\mathbf{k}_1, \mathbf{k}_2; \eta) = & \frac{(-1)^{n+1}}{2n} \times n \int d^3 \mathbf{q}_{1 \dots n} \delta_D(\mathbf{k} - \mathbf{q}_{1 \dots n}) \left\langle \left[ \frac{\delta^2 \Psi_{\rho}(\mathbf{q}_1, \eta)}{\delta \phi_a \delta \phi_b} \Psi_{\rho}(\mathbf{q}_2, \eta) \cdots \Psi_{\rho}(\mathbf{q}_n, \eta) \right] \right\rangle \\ & + (n - 1) \left\langle \frac{\delta \Psi_{\rho}(\mathbf{q}_1, \eta)}{\delta \phi_a} \frac{\delta \Psi_{\rho}(\mathbf{q}_2, \eta)}{\delta \phi_b} \Psi_{\rho}(\mathbf{q}_3, \eta) \cdots \Psi_{\rho}(\mathbf{q}_n, \eta) \right\rangle \end{aligned} \quad (40)$$

As shown in Eq. (40), the first term takes the joint average of the products of a second derivative with  $n - 1$  density fields. Diagrammatically speaking, this category includes the first, third and sixth diagram in Fig.(6), i.e. both incoming branches come from one single density field  $\Psi_{\rho}$ . The rest of the diagrams then correspond to the second term of Eq. (40), where two branches originate from two different density fields. Both terms can be written in the

$$\Gamma_A^{(2)} = \text{[Tree-level diagram]} - \frac{1}{2} \times \text{[One-loop diagram]} - 3 \times \text{[One-loop diagram]} - 2 \times \text{[One-loop diagram]} + 4 \times \text{[One-loop diagram]} - \frac{3}{2} \times \text{[One-loop diagram]} + \dots$$

**Figure 6.** Three-point nonlinear propagator  $\Gamma_A^{(2)}$  up to one-loop order, corresponding to contributions in Eq. (43) and (44).

same form of Eq. (36),

$$\begin{aligned} \Gamma_{A ab}^{(2, n)}(\mathbf{k}_1, \mathbf{k}_2; \eta) &= \sum_{\{t_{ij}\}} \int \left[ \prod_{1 \leq i < j \leq n} d^3 \mathbf{p}_{1 \dots t_{ij}}^{ij} \right] \left[ g_{\{t_{ij}\}}^{(2, n)} \Gamma_{\delta ab}^{(t_1+2)}(\mathbf{k}_1, \mathbf{k}_2; \mathbf{p}_{1 \dots t_{11}}^{11}, \dots, \mathbf{p}_{1 \dots t_{1n}}^{1n}) \times \dots \right. \\ &\quad \times \Gamma_{\delta}^{(t_n)}(\mathbf{p}_{1 \dots t_{n1}}^{n1}, \dots, \mathbf{p}_{1 \dots t_{nn}}^{nn}) + \tilde{g}_{\{t_{ij}\}}^{(2, n)} \Gamma_{\delta a}^{(t_1+1)}(\mathbf{k}_1; \mathbf{p}_{1 \dots t_{11}}^{11}, \dots, \mathbf{p}_{1 \dots t_{1n}}^{1n}) \\ &\quad \left. \times \Gamma_{\delta b}^{(t_2+1)}(\mathbf{k}_2; \mathbf{p}_{1 \dots t_{21}}^{21}, \dots, \mathbf{p}_{1 \dots t_{2n}}^{2n}) \dots \Gamma_{\delta}^{(t_n)}(\mathbf{p}_{1 \dots t_{n1}}^{n1}, \dots, \mathbf{p}_{1 \dots t_{nn}}^{nn}) \right] \prod_{1 \leq i < j \leq n} [P_0(p^{ij})]^{t_{ij}} \end{aligned} \quad (41)$$

The difference between the two terms can be clearly seen from their orders of their propagators. With the same labeling system, the first gives  $\Gamma_{\delta}^{(t_1+2)} \Gamma_{\delta}^{(t_2)} \dots \Gamma_{\delta}^{(t_n)}$ , while the second gives  $\Gamma_{\delta}^{(t_1+1)} \Gamma_{\delta}^{(t_2+1)} \dots \Gamma_{\delta}^{(t_n)}$ . Meanwhile, the two  $g$  coefficients equal

$$\begin{aligned} g_{\{t_{ij}\}}^{(2, n)} &= \frac{(-1)^{n+1}}{2} \times (t_1 + 2)(t_1 + 1) \left[ \prod_{1 \leq i \leq n} \binom{t_i}{t_{i1} \dots t_{in}} \right] \left[ \prod_{1 \leq i < j \leq n} (t_{ij})! \right], \\ \tilde{g}_{\{t_{ij}\}}^{(2, n)} &= \frac{(-1)^{n+1}}{2} \times (n-1)(t_1 + 1)(t_2 + 1) \left[ \prod_{1 \leq i \leq n} \binom{t_i}{t_{i1} \dots t_{in}} \right] \left[ \prod_{1 \leq i < j \leq n} (t_{ij})! \right]. \end{aligned} \quad (42)$$

The first contribution  $g_{\{t_{ij}\}}^{(2, n)}$  gives  $n(t_1 + 2)(t_1 + 1)$ , while the second term  $\tilde{g}_{\{t_{ij}\}}^{(2, n)}$  gives  $n(n-1)(t_1 + 1)(t_2 + 1)$ .

At tree level, there are two diagrams: one is  $\Gamma_{\delta}^{(2)}$ , from the single- $\Psi_{\rho}$  contribution; and the other is the two- $\Psi_{\rho}$  term with  $t_{12} = 0$  for the second term of Eq. (41),

$$\Gamma_{A ab}^{(2, \text{tree})}(\mathbf{p}, \mathbf{k} - \mathbf{p}; \eta) = \Gamma_{\delta ab}^{(2)}(\mathbf{p}, \mathbf{k} - \mathbf{p}; \eta) W(kR) - \frac{1}{2} \Gamma_{\delta a}^{(1)}(\mathbf{p}; \eta) \Gamma_{\delta b}^{(1)}(\mathbf{k} - \mathbf{p}; \eta) W(pR) W(|\mathbf{k} - \mathbf{p}|R). \quad (43)$$

At one-loop level, five diagrams are nonzero.

$$\Gamma_{A ab}^{(2, 1\text{-loop})}(\mathbf{p}, \mathbf{k} - \mathbf{p}; \eta) = \int d^3 \mathbf{p} P_0(q) \left[ \sum_{i=1}^5 \mathcal{K}_i^{(2, 1\text{-loop})} \right]. \quad (44)$$

where

$$\begin{aligned} \mathcal{K}_1^{(2, 1\text{-loop})} &= -3 W(qR) W(|\mathbf{k} + \mathbf{q}|R) \Gamma_{\delta}^{(1)}(-\mathbf{q}; \eta) \Gamma_{\delta ab}^{(3)}(\mathbf{k} - \mathbf{p}, \mathbf{p}, \mathbf{q}; \eta) \\ \mathcal{K}_2^{(2, 1\text{-loop})} &= -2 W(|\mathbf{p} + \mathbf{q}|R) W(|\mathbf{k} - \mathbf{p} - \mathbf{q}|R) \Gamma_{\delta a}^{(2)}(\mathbf{p}, \mathbf{q}; \eta) \Gamma_{\delta b}^{(2)}(\mathbf{k} - \mathbf{p}, -\mathbf{q}; \eta) \\ \mathcal{K}_3^{(2, 1\text{-loop})} &= 4W(qR) W(|\mathbf{p} + \mathbf{q}|R) W(|\mathbf{k} - \mathbf{p}|R) \Gamma_{\delta}^{(1)}(\mathbf{q}; \eta) \Gamma_{\delta a}^{(1)}(\mathbf{k} - \mathbf{p}; \eta) \Gamma_{\delta b}^{(2)}(\mathbf{p}, \mathbf{q}; \eta) \end{aligned}$$

$$\begin{aligned}
\mathcal{K}_4^{(2, 1\text{-loop})} &= \left[ W(qR)\Gamma_\delta^{(1)}(\mathbf{q}; \eta) \right]^2 W(kR)\Gamma_{\delta ab}^{(2)}(\mathbf{p}, \mathbf{k} - \mathbf{p}; \eta) \\
\mathcal{K}_5^{(2, 1\text{-loop})} &= -\frac{3}{2}W^2(qR)W(|\mathbf{k} - \mathbf{q}|R)W(kR) \left[ \Gamma_\delta^{(1)}(\mathbf{q}; \eta) \right]^2 \Gamma_{\delta a}^{(1)}(\mathbf{k} - \mathbf{q}; \eta)\Gamma_{\delta b}^{(1)}(\mathbf{p}; \eta).
\end{aligned} \tag{45}$$

In Eq. (45),  $\mathcal{K}_1$  and  $\mathcal{K}_2$  are two- $\Psi_\rho$  contributions from the first and second terms of Eq. (40) respectively,  $\mathcal{K}_3$  and  $\mathcal{K}_4$  are three- $\Psi_\rho$  contributions, and  $\mathcal{K}_5$  is the four- $\Psi_\rho$  contribution.

At last, the non-linear power spectrum of the log-transformed field  $\Phi_\rho$  can be expressed as

$$P_A(k; \eta) = \sum_{r \geq 1} r! \int d^3 \mathbf{q}_{1 \dots r} \delta_D(\mathbf{k} - \mathbf{q}_{1 \dots r}) \left[ \Gamma_A^{(r)}(\mathbf{q}_1, \dots, \mathbf{q}_r; \eta) \right]^2 P_0(q_1) \dots P_0(q_r). \tag{46}$$

## 5. NUMERICAL RESULTS

In this section, we show our numerical results. To simplify the calculation, we adopt the approximation Eq. (26), which has been shown to be accurate enough in Bernardeau et al. (2008). For the tree-level propagator, we only include the fastest-growing mode, i.e. the standard perturbation kernel  $F^{(n)}$ . Since the non-linear quantity  $\Gamma_\delta^{(n)}$  is involved throughout our formulae, all the calculation is done numerically. All results assume the fiducial concordance  $\Lambda$ CDM cosmology of simulation 0 of the Coyote Universe suite (Heitmann et al. 2010, 2009; Lawrence et al. 2010), with  $(\Omega_m h^2, \Omega_b h^2, n_s, w, \sigma_8, h) = (0.1296, 0.0224, 0.97, -1, 0.8, 0.72)$ . We use these parameters because we compare our perturbative results to measurements from this simulation. The linear power spectrum is calculated with the public Boltzmann code CAMB (Lewis et al. 2000), and the numerical integration is performed with the CERNLIB multi-dimensional integration routine.

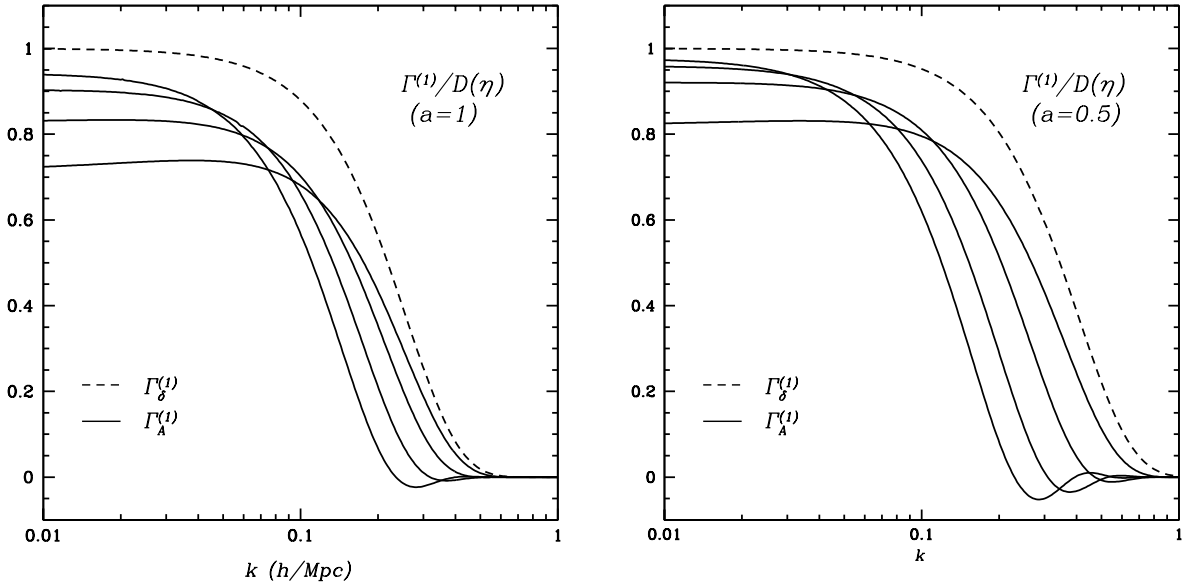


**Figure 7.** Non-linear propagator over linear growth rate at  $a = 1$  and  $a = 0.5$ . The dashed line shows the two-point propagator of the overdensity field  $\Gamma_\delta^{(1)}$ . Solid lines show the propagator for the log-transformed field  $\Gamma_A^{(1)}$ , with top-hat smoothing radius  $R = 20 h^{-1}$  Mpc,  $15 h^{-1}$  Mpc,  $10 h^{-1}$  Mpc and  $5 h^{-1}$  Mpc, from top to bottom.

In Fig.(7), we show the two-point propagator  $\Gamma_A^{(1)}(k)$  up to two-loop order. As expected from the analysis of SPT, the propagator of the  $A$  field approaches a constant less than one at large scales. The value of this large-scale bias, which also encodes the statistical information of the density fluctuation (Eq.22), strongly depends on the smoothing process adopted before the transformation. For the smoothing radius  $R \rightarrow \infty$ , effectively no loop integration contributes to  $\Gamma_A^{(1)}(k)$ , therefore the bias approaches to 1 from the tree-level result, Eq. (38). When the smoothing radius goes smaller, since  $\Gamma_\delta^{(n)}(k)$  that appears in the loop integration also decays at large  $k$ , the effect of the smoothing becomes less and less important until the bias freezes at some value, where higher-loop contributions are significant. In this sense, the presence of  $\Gamma_\delta^{(n)}(k)$  helps to regulate the convergence of the perturbative series.

At small scales,  $\Gamma_A^{(1)}(k)$  is dampened both by nonlinearities and by smoothing, while  $\Gamma_\delta^{(1)}(k)$  has no additional smoothing imposed. This is why  $\Gamma_A^{(1)}(k)$  decays at larger scales than  $\Gamma_\delta^{(1)}(k)$  for large smoothing scales. The top solid line shows  $\Gamma_A^{(1)}(k)$  with a smoothing scale  $R = 20 h^{-1}$  Mpc, which reduces to 0.5 around  $k \sim 0.1 h \text{ Mpc}^{-1}$ . As the

smoothing radius becomes smaller, the curve approaches  $\Gamma_\delta^{(1)}(k)$  at large  $k$ . For  $R = 5 h^{-1}$  Mpc (the bottom solid line), the damping of  $\Gamma_A^{(1)}(k)$  is similar to that of  $\Gamma_\delta^{(1)}(k)$ .

If the large-scale bias is divided out, boosting the  $A$  propagators to line up for small  $k$ , the  $A$  propagator may slightly exceed the  $\delta$  propagator on small scales, if the smoothing scale is sufficiently small. We have found this to be the case in preliminary simulation measurements. Disappointingly, this implies that the logarithmic transform by itself does not help appreciably to reconstruct mode-by-mode initial phases and amplitudes. But the similarity in damping is not surprising, given that e.g. bulk displacements from the initial conditions affect both fields.

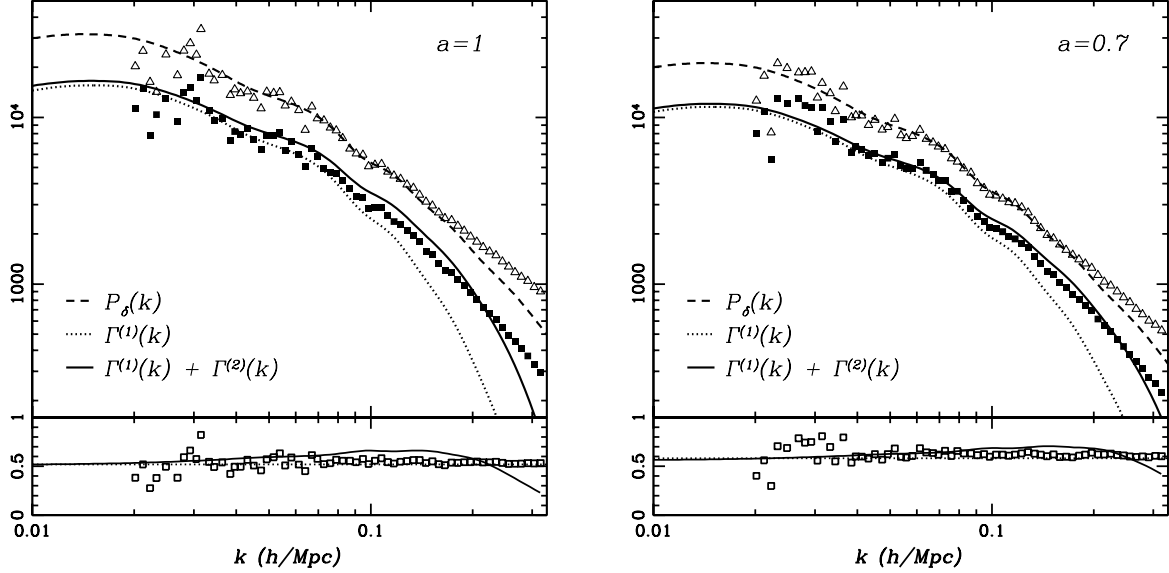


**Figure 8.** The nonlinear power spectrum of  $A = \ln(1 + \delta)$  at  $a = 1$  and  $a = 0.7$ , with top-hat smoothing radius  $R = 3.7 h^{-1}$  Mpc. *Upper panels:* Triangles and squares are the  $\delta$  and  $A$  power spectra measured from a simulation. Solid lines include both the  $\Gamma_A^{(1)}$  and  $\Gamma_A^{(2)}$  terms, and dotted lines include only the  $\Gamma_A^{(1)}$  term. Dashed lines are the linear power spectrum, damped at small scales with the NGP window function, to show the degree of nonlinearity of the  $\delta$  power spectrum. Note that we did not compute a perturbative prediction for the  $\delta$  power spectrum in this paper. *Lower panels:* the nonlinear power spectrum of  $A$  divided by the linear density power spectrum. Dotted horizontal lines indicate the value of the large scale bias. In these figures, we use a different Fourier-transform convention; compared to previous sections, here power spectra are multiplied by  $(2\pi)^3$ .

In Fig.(8), we illustrate the non-linear power spectra of both  $P_A(k)$  and  $P_\delta(k)$  at  $a = 0.7$  and  $a = 1$ . The squares and triangles are the  $\delta$  and  $A$  power spectra measured from Coyote Universe simulation 0, which has  $1024^3$  particles in a cubic 1300 Mpc ( $\sim 1 h^{-1}$  Gpc) box. Its resolution is high enough that the power spectrum is accurate to sub-percent level down to  $1 h \text{ Mpc}^{-1}$ . We measure both power spectra on  $128^3$ -cell grids, using nearest-grid-point (NGP) density assignment. Even for the  $A$  field, the shot noise is negligible at this cell size (Neyrinck et al. 2011). We do not correct either measured power spectrum for the NGP pixel window function. In fact, such a correction would be ill-defined for the  $A$  field. The dashed line shows the linear power spectrum, after applying the NGP window function. Note that we did not compute a perturbative prediction of  $P_\delta$  in this paper that would allow a fair shape comparison to our perturbative prediction of  $P_A$ .

In Fig.(9), we show the same results at redshift  $a = 0.5$ . The calculation is quite accurate before it seems to break down at  $k \sim 0.31 h \text{ Mpc}^{-1}$ . In the inside panel, we show the BAO wiggles of both  $P_A(k)$  and linear  $P_\delta(k)$ , dividing out the Eisenstein & Hu (1998) ‘no-wiggle’ power spectrum.

The PT result of  $P_A(k)$  (solid line) includes contributions from  $\Gamma_A^{(1)}$  as well as  $\Gamma_A^{(2)}$ . Since the numerical integration involving  $\Gamma_A^{(2)}$  becomes extremely time-consuming, we only calculate it up to one-loop order, while  $\Gamma_A^{(1)}$  is done to two-loop order. The agreement with the data measured from simulation is good, given the several approximations we have made. For  $a = 1$ , the calculation breaks down after  $k \gtrsim 0.2 h \text{ Mpc}^{-1}$ . Also, the discrepancy with data between  $k = 0.1$  and  $k = 0.2 h \text{ Mpc}^{-1}$  peaks at over 10%. This is where  $\Gamma_A^{(2)}$  becomes dominant, but is only calculated up to one-loop order. The dotted line presents the  $\Gamma_A^{(1)}$  contribution. For higher redshifts, the differences between data and theory become smaller. At  $a = 0.7$ , the prediction breaks down around  $k \sim 0.28 h \text{ Mpc}^{-1}$ . In the lower panel of each figure, we also plot the ratio between  $P_A(k)$  and the linear power spectrum, after applying the pixel window function.

## 6. CONCLUSION

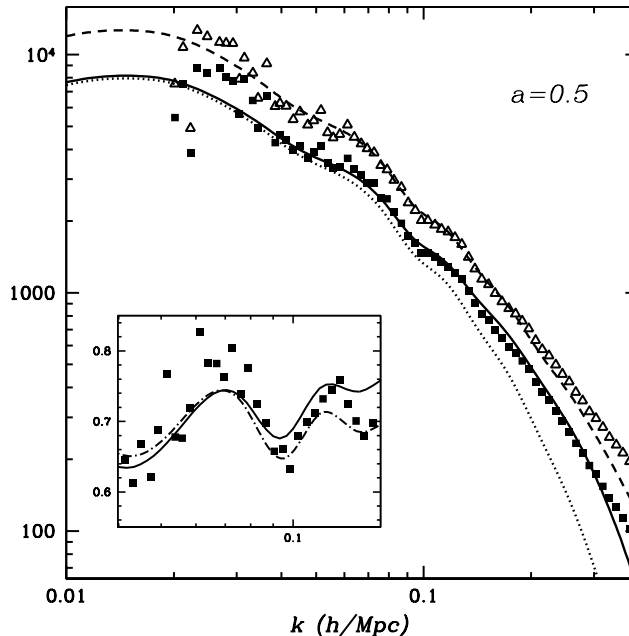


**Figure 9.** The nonlinear power spectrum of  $A = \ln(1 + \delta)$ , at  $a = 0.5$ , with top-hat smoothing radius  $R = 3.7 h^{-1}$  Mpc. Linestyles and symbols the same as in Fig. 8. *Inset:* The solid line shows the BAO wiggles of  $P_A(k)$ , dividing out the Eisenstein & Hu (1998) ‘no-wiggle’ power spectrum. The dot-dashed line presents the wiggleness of the linear  $P_\delta(k)$ , multiplied by a constant to line up with  $P_A(k)$  at large scales.

In this paper, we developed the cosmological perturbation theory for the log-density field  $A = \ln(1 + \delta)$ . In the context of standard perturbation theory, we showed how different smoothing scales can alter the amplitude of the  $A$  power spectrum at large scales. With the help of multi-point propagators developed in renormalized perturbation theory, we constructed the building blocks for the power spectrum of the  $A$  field. In our formalism, each diagram effectively includes infinitely many loop contributions. The Gaussian damping of the propagator for the  $A$  field ensures that the convergence of the series is well-controlled.

We found that except for the large-scale bias, this  $A$  propagator, which quantifies the memory of initial conditions as a function of scale, is similar to the  $\delta$  propagator, damping at a similar length scale. This means that the memory of mode-by-mode initial phases and amplitudes in the  $A$  field is not much better than in the  $\delta$  field.

Even with several approximations, our PT calculation for  $P_A$  achieves good agreement with simulation measurements. However, further work is necessary to obtain results with sufficient precision to resolve the question of whether the much-reduced nonlinearity in the shape of  $P_A$  compared to  $P_\delta$  is understandable perturbatively.

We thank Katrin Heitmann and Adrian Pope for help accessing the Coyote Universe simulations. XW, MN and AS are grateful for support from the W.M. Keck and the Gordon and Betty Moore Foundations, and IS from NASA grants NNG06GE71G and NNX10AD53G, and from the Polányi Program of the Hungarian National Office for Research and Technology (NKTH).

## APPENDIX

### Appendix A. ONE-LOOP SPT

In this appendix, we present the one-loop result of  $P_A(k)$  in the context of standard perturbation theory. Starting from Eq. (19), if one only considers the fastest-growing mode,  $2P_A^{(13)}$  becomes

$$2P_A^{(13)}(k, \eta) = 2P_\delta^{(13)}(k, \eta)W^2(kR) + 2\sigma_R^2 P_L(k, \eta)W^2(kR) - 4 \left[ \int d^3 \mathbf{p} P_L(p, \eta) F^{(2)}(\mathbf{k}, \mathbf{p}) W(pR) W(|\mathbf{k} + \mathbf{p}|R) \right] P_L(k, \eta) W(kR), \quad (\text{A1})$$

where we have already expressed the four-point joint average in terms of the power spectrum.  $F^{(2)}(\mathbf{k}_1, \mathbf{k}_2) = \frac{5}{7} + \frac{1}{2}\mu \left( \frac{k_1}{k_2} + \frac{k_2}{k_1} \right) + \frac{2}{7}\mu^2$  is the second order perturbation kernel, where  $\mu = \frac{\mathbf{k}_1 \cdot \mathbf{k}_2}{k_1 k_2}$ . It can be further simplified by integrating

out the angular part of the third term of Eq. (A1)

$$\int d\Omega_p \left[ 1 + \frac{1}{2}\mu\left(\frac{p}{k} + \frac{k}{p}\right) - \frac{2}{7}(1 - \mu^2) \right] W(|\mathbf{k} + \mathbf{p}|R), \quad (\text{A2})$$

where  $\mu$  is the cosine of the angle between the vectors  $\mathbf{k}$  and  $\mathbf{p}$ . To proceed, let us consider the spherical top-hat window function, which in Fourier space is defined as

$$W_{th}(kR) = \frac{3}{(kR)^3} [\sin(kR) - kR \cos(kR)]. \quad (\text{A3})$$

For a given vector  $\mathbf{k}$ , one can prove the following integration identities (Bernardeau 1994a,b, 1996):

$$\int \frac{d\Omega_p}{4\pi} (1 - \mu^2) W_{th}(|\mathbf{k} + \mathbf{p}|R) = \frac{2}{3} W_{th}(kR) W_{th}(pR); \quad (\text{A4})$$

$$\begin{aligned} \int \frac{d\Omega_p}{4\pi} \left[ 1 + \frac{1}{2}\mu\left(\frac{k}{p} + \frac{p}{k}\right) \right] W_{th}(|\mathbf{k} + \mathbf{p}|R) &= \frac{1}{2} \left[ \frac{\sin(pR)}{pR} W_{th}(kR) + \frac{\sin(kR)}{kR} W_{th}(pR) \right] = W_{th}(kR) W_{th}(pR) \\ &+ \frac{1}{6} [W_{th}(kR) pR W'_{th}(pR) + W_{th}(pR) kR W'_{th}(kR)] \end{aligned} \quad (\text{A5})$$

Substituting Eqs.(A4 & A5) into Eq. (A2), one obtains

$$\begin{aligned} 2P_A^{(13)}(k, \eta) &= 2P_\delta^{(13)}(k, \eta) W^2(kR) - \frac{26}{21} \sigma_R^2 P_L(k, \eta) W^2(kR) - \frac{2}{3} \left[ \int dp 4\pi p^3 R P_L(p, \eta) \right. \\ &\quad \left. \times W_{th}(pR) W'_{th}(pR) \right] P_L(k, \eta) W_{th}^2(kR) - \frac{2}{3} \sigma_R^2 [kR W'_{th}(kR) W_{th}(kR)] P_L(k, \eta), \end{aligned} \quad (\text{A6})$$

which reduces to Eq. (20) if we define the derivative of  $\sigma_R^2$  with respect to  $R$ , Eq (21). As for  $P_A^{(22)}(k)$ , one can derive

$$\begin{aligned} P_A^{(22)}(k, \eta) &= P_\delta^{(22)}(k, \eta) W^2(kR) + \int d^3\mathbf{p} P_L(p, \eta) P_L(|\mathbf{k} - \mathbf{p}|, \eta) \left[ \frac{1}{2} W^2(pR) W^2(|\mathbf{k} - \mathbf{p}|R) \right. \\ &\quad \left. - F^{(2)}(\mathbf{p}, \mathbf{k} - \mathbf{p}) W(pR) W(|\mathbf{k} - \mathbf{p}|R) W(kR) \right] \end{aligned} \quad (\text{A7})$$

## Appendix B. GEOMETRIC PROPERTIES OF THE TOP-HAT WINDOW FUNCTION

Integration identities Eq. (A4) and Eq. (A5) are nearly the same as the one derived in the Appendix of Bernardeau (1994a,b), except only one angular integration is involved. Following Bernardeau (1994a,b), the top-hat window function can be decomposed as a sum of Bessel functions

$$\begin{aligned} W_{th}(k) &= 3\sqrt{\pi/2} k^{-3/2} J_{3/2}(k) \\ W_{th}(|\mathbf{k} + \mathbf{p}|) &= 3\pi \sum_{m=0}^{\infty} \left(\frac{3}{2} + m\right) (kp)^{-3/2} J_{3/2+m}(k) J_{3/2+m}(p) \frac{d}{d\mu} \mathcal{P}_{m+1}(-\mu), \end{aligned} \quad (\text{B1})$$

where  $\mathcal{P}_m$  is the Legendre polynomial of order  $m$ . Therefore Eq. (A4) can be expressed as

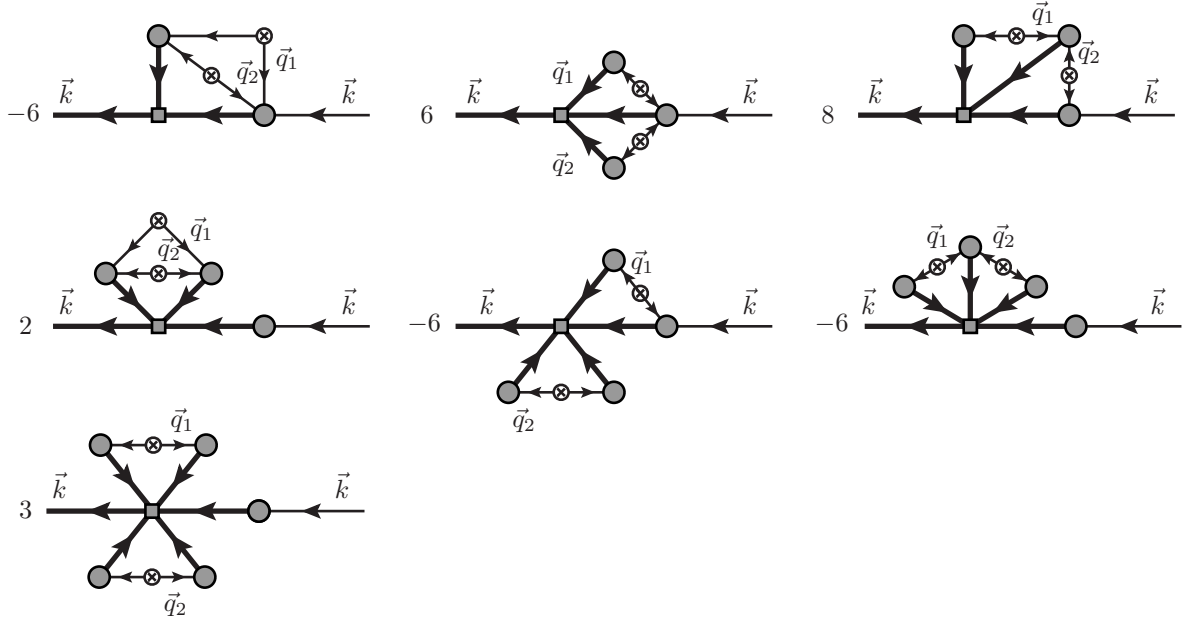
$$\int \frac{d\Omega_p}{4\pi} (1 - \mu^2) W_{th}(|\mathbf{k} + \mathbf{p}|) = \frac{3\pi}{2} \sum_{m=0}^{\infty} \left(\frac{3}{2} + m\right) (kp)^{-3/2} J_{3/2+m}(k) J_{3/2+m}(p) \int_{-1}^1 d\mu (1 - \mu^2) \frac{d}{d\mu} \mathcal{P}_{m+1}(-\mu). \quad (\text{B2})$$

Since  $\int_{-1}^1 d\mu (1 - \mu^2) \frac{d}{d\mu} \mathcal{P}_{m+1}(-\mu) = \frac{4}{3} \delta_{0m}$ , Eq. (A4) is proved.

$$\int \frac{d\Omega_p}{4\pi} (1 - \mu^2) W_{th}(|\mathbf{k} + \mathbf{p}|) = 3\pi (kp)^{-3/2} J_{3/2+m}(k) J_{3/2+m}(p) = \frac{2}{3} W_{th}(k) W_{th}(p). \quad (\text{B3})$$

For Eq. (A5), by substituting  $x = |\mathbf{k} + \mathbf{p}|R$ , one gets

$$\frac{3}{2} \int_{|\mathbf{k}-\mathbf{p}|R}^{|\mathbf{k}+\mathbf{p}|R} \frac{x dx}{kpR^2} \left[ 1 + \frac{(k^2 + p^2)(x^2/R^2 - k^2 - p^2)}{4k^2p^2} \right] \frac{\sin(x) - x \cos(x)}{x^3} = \frac{1}{2} \left[ W(kR) \frac{\sin(pR)}{pR} + W(pR) \frac{\sin(kR)}{kR} \right]. \quad (\text{B4})$$

Appendix C. TWO-LOOP ORDER OF  $\Gamma_A^{(1)}$ 

**Figure 10.** Two-loop order of the two-point nonlinear propagator.

In this paper, we have calculated the two-point propagator  $\Gamma_A^{(1)}$  up to two-loop order. Seven non-vanishing contributions are depicted in Fig.(10). From these diagrams, one can write down all terms explicitly

$$\Gamma_{A a}^{(1, 2\text{-loop})}(\mathbf{k}; \eta) = \int d^3 \mathbf{p}_{12} P_0(p_1) P_0(p_2) \left[ \sum_{i=1}^7 \mathcal{K}_i^{(1, 2\text{-loop})} \right] \quad (\text{C1})$$

where

$$\begin{aligned} \mathcal{K}_1^{(1, 2\text{-loop})} &= -6 W(|\mathbf{p}_1 + \mathbf{p}_2|R) W(|\mathbf{k} + \mathbf{p}_1 + \mathbf{p}_2|R) \Gamma_\delta^{(2)}(-\mathbf{p}_1, -\mathbf{p}_2; \eta) \Gamma_{\delta a}^{(3)}(\mathbf{k}, \mathbf{p}_1, \mathbf{p}_2; \eta), \\ \mathcal{K}_2^{(1, 2\text{-loop})} &= 6 W(p_1 R) W(p_2 R) W(|\mathbf{k} + \mathbf{p}_1 + \mathbf{p}_2|R) \Gamma_\delta^{(1)}(-\mathbf{p}_1; \eta) \Gamma_\delta^{(1)}(-\mathbf{p}_2; \eta) \Gamma_{\delta a}^{(3)}(\mathbf{k}, \mathbf{p}_1, \mathbf{p}_2; \eta), \\ \mathcal{K}_3^{(1, 2\text{-loop})} &= 8 W(p_1 R) W(|\mathbf{p}_1 + \mathbf{p}_2|R) W(|\mathbf{k} - \mathbf{p}_2|R) \Gamma_\delta^{(2)}(\mathbf{p}_1, \mathbf{p}_2; \eta) \Gamma_\delta^{(1)}(-\mathbf{p}_1; \eta) \Gamma_{\delta a}^{(2)}(\mathbf{k}, -\mathbf{p}_2; \eta) \\ \mathcal{K}_4^{(1, 2\text{-loop})} &= 2 W^2(|\mathbf{p}_1 + \mathbf{p}_2|R) W(k R) \Gamma_\delta^{(2)}(\mathbf{p}_1, \mathbf{p}_2; \eta) \Gamma_\delta^{(2)}(-\mathbf{p}_1, -\mathbf{p}_2; \eta) \Gamma_{\delta a}^{(1)}(\mathbf{k}; \eta) \\ \mathcal{K}_5^{(1, 2\text{-loop})} &= -6 W(p_1 R) W^2(p_2 R) W(|\mathbf{k} - \mathbf{p}_1|R) \Gamma_\delta^{(1)}(\mathbf{p}_1; \eta) \left[ \Gamma_\delta^{(1)}(\mathbf{p}_2; \eta) \right]^2 \Gamma_{\delta a}^{(2)}(\mathbf{k}, -\mathbf{p}_1; \eta) \\ \mathcal{K}_6^{(1, 2\text{-loop})} &= -6 W(k R) W(p_1 R) W(p_2 R) W(|\mathbf{p}_1 + \mathbf{p}_2|R) \Gamma_\delta^{(2)}(\mathbf{p}_1, \mathbf{p}_2; \eta) \Gamma_\delta^{(1)}(-\mathbf{p}_1; \eta) \Gamma_\delta^{(1)}(-\mathbf{p}_2; \eta) \Gamma_{\delta a}^{(1)}(\mathbf{k}; \eta) \\ \mathcal{K}_7^{(1, 2\text{-loop})} &= 3 W^2(p_1 R) W^2(p_2 R) W(k R) \left[ \Gamma_\delta^{(1)}(\mathbf{p}_1; \eta) \right]^2 \left[ \Gamma_\delta^{(1)}(\mathbf{p}_2; \eta) \right]^2 \Gamma_{\delta a}^{(1)}(\mathbf{k}; \eta) \end{aligned} \quad (\text{C2})$$

## REFERENCES

- Bernardeau, F., 1994a, ApJ, 427, 51  
 Bernardeau, F., 1994b, ApJ, 433, 1  
 Bernardeau, F., 1996, A&A, 312, 11  
 Bernardeau, F., Crocce, M., Scoccimarro, R., 2008, PRD, 78, 103521  
 Coles, P., Jones, B., 1991, MNRAS, 248, 1.  
 Crocce, M., Scoccimarro, R., 2006, PRD, 73, 063519.  
 Crocce, M., Scoccimarro, R., 2006, PRD, 73, 063520.  
 Crocce, M., Scoccimarro, R., 2008, PRD, 77, 023533.  
 Eisenstein, D. J., Hu, W, 1998, ApJ, 496, 605.  
 Hamilton, A. J. S. 1985, ApJ, 292, L35  
 Heitmann, K., Higdon, D., White, M., Habib, S., Williams, B. J., Lawrence, E., & Wagner, C. 2009, ApJ, 705, 156  
 Heitmann, K., White, M., Wagner, C., Habib, S., & Higdon, D. 2010, ApJ, 715, 104  
 Hubble, E. 1934, ApJ, 79, 8

- Kofman, L., Bertschinger, E., Gelb, J. M., Nusser, A., & Dekel, A. 1994, ApJ, 420, 44  
Lawrence, E., Heitmann, K., White, M., Higdon, D., Wagner, C., Habib, S., & Williams, B. 2010, ApJ, 713, 1322  
Lewis, A., Challinor, A., & Lasenby, A. 2000, ApJ, 538, 473, <http://www.camb.info/>  
Matsubara, T., 2008, MNRAS, 77, 063530  
Neyrinck, M. C., Szapudi, I., & Szalay, A. S. 2009, ApJ, 698, L90  
Neyrinck, M. C., Szapudi, I., & Szalay, A. S. 2011, ApJ, 731, 116  
Pietroni, M., 2008, JCAP, 10, 36.  
Smith, R. E., et al. 2003, MNRAS, 341, 1311  
Springel, V., et al. 2005, Nature, 435, 629  
Szapudi, I., Kaiser, N., 2003, ApJ, 583, L1.  
Taruya, A., Hiramatsu, T., 2008, ApJ, 674, 617.